

Investigation of the Enhanced Lithium Battery Storage in a Polyoxometalate Model: From Solid Spheres to Hollow Balls

Wen-Jing Liu, Ge Yu, Mi Zhang, Run-Han Li, Long-Zhang Dong, Hui-Si Zhao, Yong-Jun Chen, Zhi-Feng Xin, Shun-Li Li, and Ya-Qian Lan*

Materials with hollow structures are generally considered more conducive to lithium-ion storage than solid materials, but there is no suitable crystal model system to illustrate it. Herein, it is successfully simulated by utilizing polyoxometalate models to compare the lithium-ion battery performances. New crystals, EMI-PMo₁₂ (EMI: 1-ethyl-3-methylimidazolium) with solid sphere and EMI-Mo₇₂V₃₀ and EMI-Mo₁₃₂ with hollow structures, are synthesized. In order to increase their electronic conductivity, the composites EMI-PMo₁₂@rGO, EMI-Mo₇₂V₃₀@rGO, and EMI-Mo₁₃₂@rGO (rGO: reduced graphene oxide) can be prepared by introducing rGO. The composite EMI-Mo₇₂V₃₀@rGO delivers a reversible capacity of 1145 mAh g⁻¹ at 100 mA g⁻¹, and the capacity retentions are nearly 100% at 2000 mA g⁻¹ for over 500 cycles. This study not only provides a promising avenue toward manufacturing and developing new-generation electrode materials in lithium-ion storage but also proposes a mechanism toward comparing their performances at the molecular level.

Meanwhile, various complex hollow structures have been prepared with the goal of exposing more active sites, but their battery storage mechanisms have not been well studied at the molecular level. If metal clusters and hollow metal molecular balls with defined structures in different sizes could be synthesized, and their battery performances could be compared to tell the differences between solid nanoparticles and hollow structures, we could better understand the battery storage mechanism at the molecular level, and further provide us a guidance on the design and synthesis of new battery electrode materials. However, it is still a great challenge to find such a molecular model, especially a system containing single-crystal structures. Such a modeling system requires both solid metal clusters and hollow metal structures to be

stable and with excellent redox abilities to better simulate the existing battery electrode solid materials.

Polyoxometalates (POMs), resulting from the aggregation of multimetal oxoanions bearing complexing functions, which can reversibly accept and lose electrons without changing their structures,^[40–46] are important candidates for battery electrode material. POMs have aesthetically beautiful structures ranging in size from about 1 nm (e.g., Keggin, solid sphere without voids, Scheme 1a) to 2–5 nm (e.g., Mo₇₂V₃₀ and Mo₁₃₂, hollow metal ball, Scheme 1b).^[47,48] Therefore, POM clusters and hollow ball structures provide us a perfect modeling system that allows us to simulate macroscopic metal oxide particles and the hollow nanomaterials at the molecular level for comparing Li⁺ storage performance. To the best of our knowledge, no examples have been reported so far. However, the main obstacle for applying POMs directly in LIBs is their high solubility in electrolyte and their low electronic conductivity.^[49,50] To address these issues, one of the most popular methods is to immobilize POMs evenly on some carbon materials, such as reduced graphene oxide (rGO), which not only provides large surface area but also improves the conductivity.^[51–57] Nevertheless, the interaction between polyanion POMs and negatively charged carbon supported rGO is weak. Hence, POMs fall off easily from rGO and their stabilities are diminished. Therefore, the design and introduction of efficient connector to bridge POMs and rGO are important. To solve this problem, the multifunctional ionic liquid (1-ethyl-3-methylimidazolium bromide, EMI-Br) was chosen as a positively charged ionic conducting

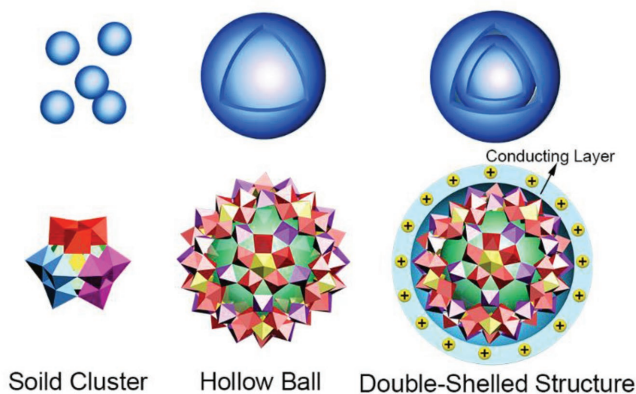
1. Introduction

Lithium-ion batteries (LIBs) are widely used in portable electronics and energy-storage devices.^[1–10] Traditional metal oxide anode materials including Fe₃O₄, SnO₂, Li₄Ti₅O₁₂, etc. are synthesized with solid particle morphology,^[11–15] which cannot meet the rapid ever-growing demands on the energy density of LIBs. Therefore, the development of novel efficient hollow materials with tunable porosity and high surface is highly desired.^[16] Hollow structured metal oxides with Co₃O₄,^[17] CuO@NiO,^[18] CoMn₂O₄,^[19] Fe₂O₃,^[20] TiO₂,^[21,22] etc. have garnered tremendous interest due to their fascinating physicochemical properties, which could be beneficial for the enhancement of Li⁺ storage performance. These hollow or multishelled structures are ranging in size from a few hundred nanometers to micrometers.^[23–39]

Dr. W.-J. Liu, G. Yu, Dr. M. Zhang, R.-H. Li, L.-Z. Dong, H.-S. Zhao, Y.-J. Chen, Prof. Z.-F. Xin, Prof. S.-L. Li, Prof. Y.-Q. Lan
Jiangsu Collaborative Innovation Centre of Biomedical Functional Materials
Jiangsu Key Laboratory of New Power Batteries
School of Chemistry and Materials Science
Nanjing Normal University
Nanjing 210023, P. R. China
E-mail: yqlan@njnu.edu.cn

The ORCID identification number(s) for the author(s) of this article can be found under <https://doi.org/10.1002/smt.201800154>.

DOI: 10.1002/smt.201800154



Scheme 1. Schematic illustration of a) the solid cluster; and b) hollow structure with interior cavity, by utilizing POM molecular model; c) double-shelled EMI-POM structure with the inherent porosity and the outer ionic conducting layer EMI (yellow ball).

layer (Scheme 1c) to scaffold POMs and rGO. Polyanion POMs encapsulated with cationic EMI to form EMI-POMs composites not only suppress the solubility of POMs in electrolyte but also enhance electroconductivity of POMs.^[58] Simultaneously, the imidazolium rings of EMI could be apprehended on the surface plane of rGO by ionic bonding and π - π stacking interaction.^[59,60] The synergistic effect of POMs, EMI, and rGO plays a key role in the formation of new materials.

Herein, we report on the synthesis and characterization of a class of composites, all of which are solid spheres or hollow ball-shaped POMs encapsulated by EMI on rGO, namely, EMI-PMo₁₂@rGO, EMI-Mo₇₂V₃₀@rGO, and EMI-Mo₁₃₂@rGO. The giant POMs were chosen as precursors to prepare anode materials for the first time based on the following considerations: First, POM balls combine the advantage of well-defined structures and inherent existence of many transition metal oxides in one molecular, which could be helpful for understanding the discharge/charge mechanism at the molecular level. Second, the macrocyclic structures have 20 open pore windows which can be used to enter and leave freely, charge-balancing Li⁺ cations inside the pores, resulting in the enhanced Li⁺ storage inside pores. Third, the fullerene-like structures not only have high specific area but also have an interior cavity which could provide free space, avoid strain relaxation and volume expansion during the repeated Li⁺ intercalation-deintercalation process. Besides, EMI acts as ion conducting layer that facilitates the transportation of Li⁺ between POM molecules, together with the increased electronic conductivity provided by rGO, ensuring the improvement of cycling and rate performance. Last but not the least, EMI-POMs with precise structures and the maximum number of Li⁺ inserted inside its pores could be calculated, providing us a better understanding of the storage mechanism. As expected, the EMI-Mo₇₂V₃₀@rGO composite retains a high capacity of 1145 mAh g⁻¹ at a current density of 100 mA g⁻¹ without significant cycling fading over 100 cycles, and tolerates a long-term cycling up to 500 cycles at the current density of 2000 mA g⁻¹. The detailed mechanism and differences for Li⁺ storage between solid POM cluster and hollow POM cages are discussed. This study has reference for other solid-state electrode materials for Li⁺ storage.

2. Results

2.1. Synthesis and Characterization

The single crystals EMI-PMo₁₂, EMI-Mo₇₂V₃₀, and EMI-Mo₁₃₂ were synthesized by interaction of the respective POM anions and EMI as counter cation using hydrothermal routes at 130 °C and were characterized by single-crystal X-ray diffraction (XRD) structure analyses, inductively coupled plasma analyses (ICP), elemental analyses (EA), the Fourier transform infrared spectra (FTIR), and thermogravimetry (TGA) (see Tables S1–S3, Supporting Information). {PMo₁₂} is composed of a central {PO₄} tetrahedron surrounded by four corner-shared {Mo₃O₁₃} groups, forming a tightly packed solid cluster (Figure 1a). {Mo₇₂V₃₀} is constituted of 12 {(Mo^{VI})Mo^{VI}₅} pentagonal bipyramids and 30 {V^{IV}O} as linkers to build a nanocage with the diameter of 21 Å (Figure 1b).^[61] As shown in Figure 1c, {Mo₁₃₂} consists of 12 pentagonal units and 30 {Mo^V₂} as linkers, resulting a hollow ball with the pore size of 25 Å in diameter.^[47] By calculation based on EA, ICP, and TGA data, the numbers of EMI contained in each single cell of EMI-PMo₁₂, EMI-Mo₇₂V₃₀, and EMI-Mo₁₃₂ are 3, 20, and 22, respectively. From the 3D structure charts, we see that each POM is surrounded by an EMI layer (Figures S1–S3, Supporting Information). The EMI-POM@rGO composites were prepared under the reaction conditions similar to the above but by introducing GO. Notably, GO is reduced to rGO due to the redox ability of POMs under the high reaction temperature. The powder XRD peaks (Figure 1d–f) of EMI-POMs and EMI-POM@rGO agree with the corresponding simulated peaks, indicating that the stable EMI-POMs keep their structure intact after introducing rGO. The FTIR and Raman spectra further prove the fact that the EMI-POM@rGO composites keep the structural integrity of POMs in terms of no movement of the absorption bands of Mo=O, V=O, and Mo–O–Mo (Figures S4 and S5, Supporting Information).

As shown in Figure 2a,c, the scanning electron microscopy (SEM) and transmission electron microscopy (TEM) of EMI-Mo₇₂V₃₀@rGO reveal that the EMI-Mo₇₂V₃₀ structures with regular nanoflake-like morphology are loaded on the rGO nanosheets. Figure 2b shows the schematic diagram of EMI-POM@rGO. High-resolution TEM (HRTEM) (Figure 2d) of a piece of the flake displays nanoball shape. Besides, the selected-area electron diffraction (SAED) pattern shows that the neatly arranged spots are associated with those of the simulated single crystal's spots, indicating the single-crystal nature of EMI-Mo₇₂V₃₀ (inset in Figure 2c and Figure S6a, Supporting Information). The lattice space of 1.72 nm can be indexed to the (110) plane of EMI-Mo₇₂V₃₀ (HRTEM, Figure S6b, Supporting Information). The mapping results of EMI-Mo₇₂V₃₀@rGO and EMI-Mo₇₂V₃₀ (Figure 2e and Figure S6c, Supporting Information) show that the corresponding elements are uniformly distributed. The SEM, TEM, HRTEM images, and elemental mapping of these composites are shown in Figures S7–S10 (Supporting Information). It is very interesting that the morphologies of those single crystals are consistent with that of the compound after grafting with graphene (Figure S8, Supporting Information). The TGA (Figure S11, Supporting Information) combined with the elemental analysis results of single crystal

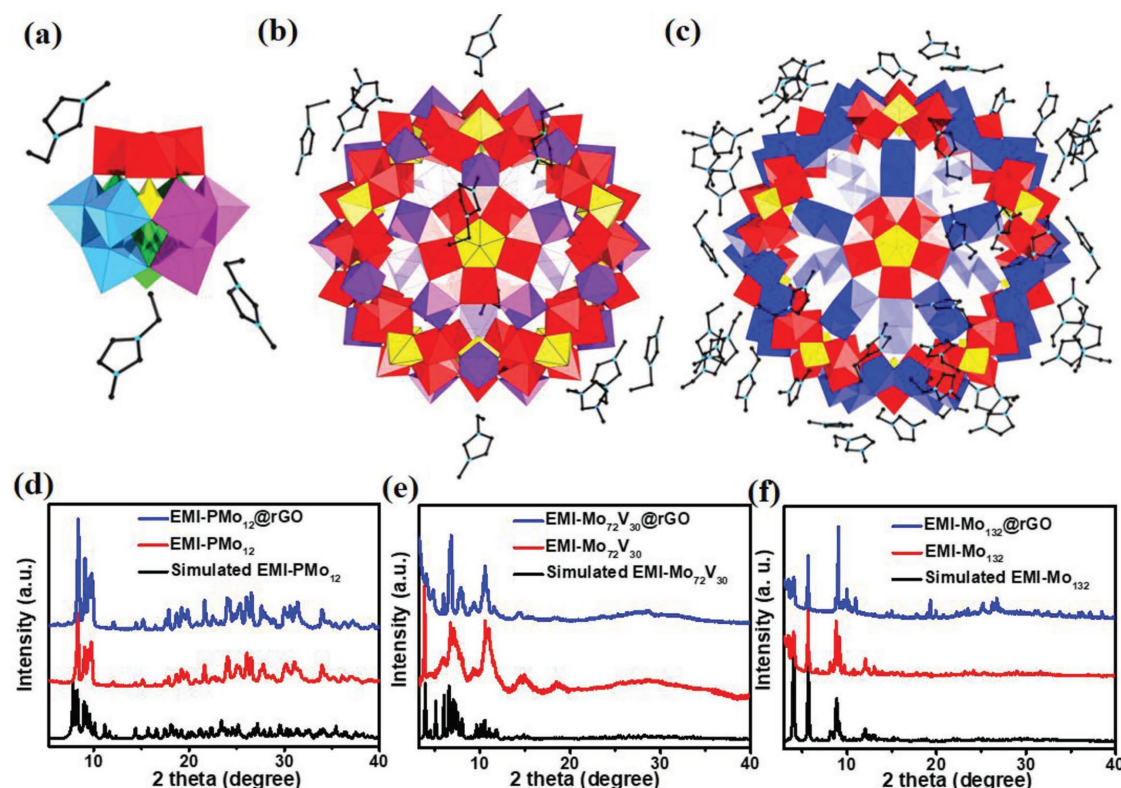


Figure 1. Combined polyhedral and ball-and-stick representation of a) EMI-PMo₁₂, b) EMI-Mo₇₂V₃₀, and c) EMI-Mo₁₃₂; XRD patterns of d) PMo₁₂, EMI-PMo₁₂, and EMI-PMo₁₂@rGO; e) Mo₇₂V₃₀, EMI-Mo₇₂V₃₀, and EMI-Mo₇₂V₃₀@rGO; and f) Mo₁₃₂, EMI-Mo₁₃₂, and EMI-Mo₁₃₂@rGO.

materials are used to calculate the amount of guest crystal water. TGA results also demonstrate that the composites have good thermal stability, and the dehydrated composites could be obtained after dried at 100 °C. The N₂ adsorption-desorption isotherms analyses show that the composites with mesoporous structure exhibit a higher specific surface area than that of the single-crystalline materials (e.g., EMI-Mo₇₂V₃₀@rGO: 76.6 m² g⁻¹, EMI-Mo₇₂V₃₀: 37.4 m² g⁻¹), benefiting the improved lithium diffusion and intercalation (Figure S12, Supporting Information).

2.2. Electrochemistry Performances

The LIB anode performance of as-synthesized composites was evaluated in half-cell configurations. The single crystals EMI-Mo₇₂V₃₀ show better capacity performance than EMI-PMo₁₂ and EMI-Mo₁₃₂, corresponding to the reversible capacities of 824.6 mAh g⁻¹ at 100 mA g⁻¹ after 100 cycles, which is higher than 242.8 mAh g⁻¹ of EMI-PMo₁₂ and 440.3 mAh g⁻¹ of EMI-Mo₁₃₂ (Figure 3a). After these crystals immobilized on rGO, the cycling performance of the as-synthesized EMI-POM@rGO composites has been greatly improved (Figure 3b). The reversible capacity of EMI-Mo₇₂V₃₀@rGO is preserved at over 1150 mAh g⁻¹ at 100 mA g⁻¹ for at least 100 cycles with capacity retention nearly 100%, whereas that of EMI-PMo₁₂@rGO and EMI-Mo₁₃₂@rGO are 343.3 and 870.9 mAh g⁻¹, respectively. Figure 3c shows that the first charge-discharge

capacity of EMI-Mo₇₂V₃₀@rGO is 2046.2 and 1397.3 mAh g⁻¹, and the Coulomb efficiency is 68.3%, which is better than EMI-PMo₁₂@rGO (35.4%) and EMI-Mo₁₃₂@rGO (64.4%). The capacities of EMI-POM@rGO at different current densities are shown in Figure 3d. The capacities of EMI-Mo₇₂V₃₀@rGO are 1082.5, 988.2, 804.6, 691.1, 564.6, 482.2, and 371.1 mAh g⁻¹ at the current densities of 100, 200, 500, 1000, 2000, 3000, and 5000 mA g⁻¹, respectively. When the current rates have been changed back to 1000 and 100 mA g⁻¹ successively, the high capacities of 809.6 and 1162.4 mA g⁻¹ were resumed, suggesting the fairly stable capacitance. Figure 3e shows that the EMI-Mo₇₂V₃₀@rGO has a stable capacity of 590.9 mAh g⁻¹ after 500 cycles at a current density of 2 A g⁻¹. It is one of the best high-performance electrodes among the reported POM-based materials (Table S4, Supporting Information). The photographs of solubility test (Figure S13, Supporting Information) demonstrate that the introduction of EMI and rGO not only solves the problem of POM dissolving in electrolyte but also enhances their stability. The composite EMI-Mo₇₂V₃₀@rGO shows better performance than the crystals EMI-Mo₇₂V₃₀, Mo₇₂V₃₀ and the composite Mo₇₂V₃₀@rGO (without EMI), indicating that synergistic effect of the conductive rGO, Li⁺ conductor EMI, and the giant POM plays a key role in enhancing Li⁺ storage (Figure S14a, Supporting Information). The comparative cycling performance of the composite EMI-Mo₇₂V₃₀@rGO with different GO loading concentrations at a current density of 100 mA g⁻¹ was also studied in Figure S14b (Supporting Information). The detailed electrochemical performances of

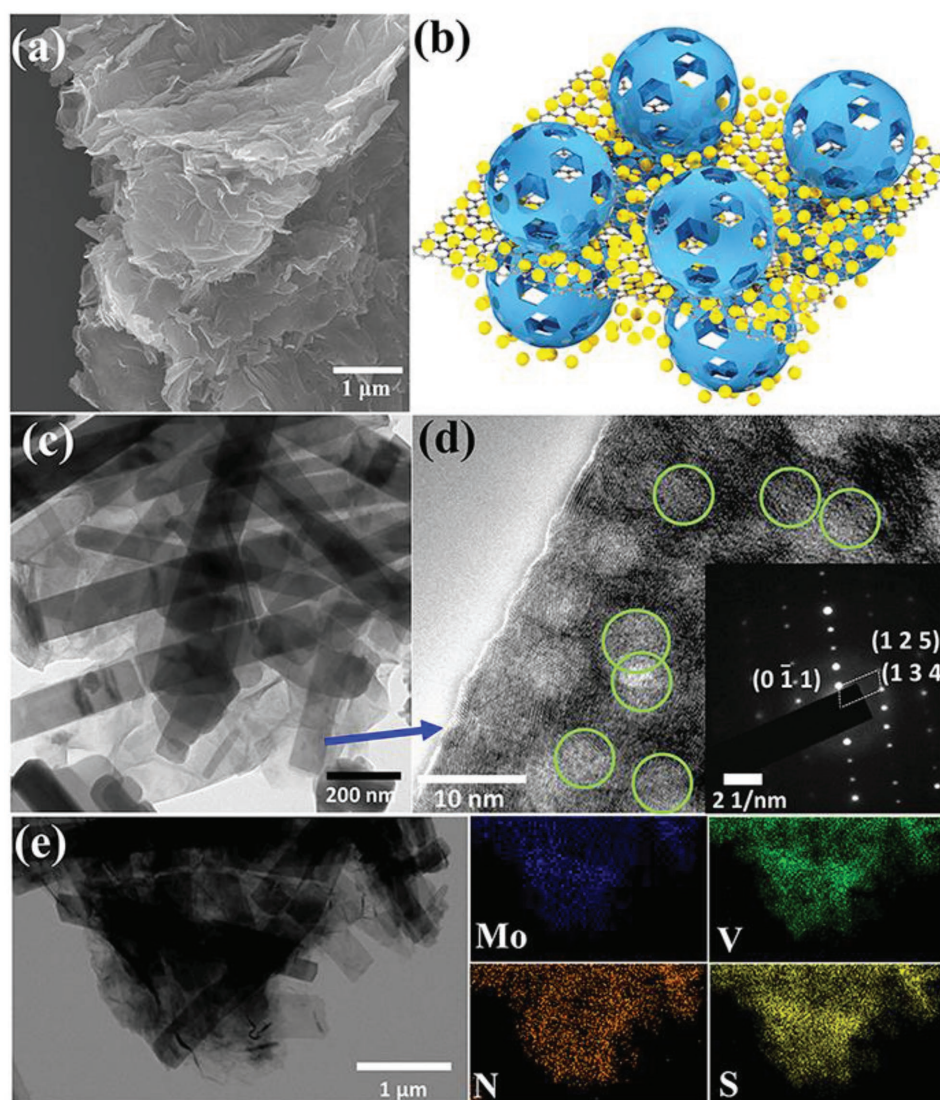


Figure 2. a) SEM images of EMI-Mo₇₂V₃₀@rGO composite; b) schematic diagram of EMI-Mo₇₂V₃₀@rGO (the yellow balls represent EMI, the giant blue balls represent Mo₇₂V₃₀); c) TEM images of EMI-Mo₇₂V₃₀@rGO composite; d) HRTEM image and SAED pattern of the corresponding piece of EMI-Mo₇₂V₃₀; e) bright-field STEM images of EMI-Mo₇₂V₃₀@rGO; EDX mapping images of Mo, V, S, and N elements.

those compounds are discussed in Figures S14–S16 (Supporting Information). The morphologies of EMI-Mo₇₂V₃₀@rGO electrode were performed before and after cycling (measured at 0.01 and 3 V vs Li/Li⁺) to investigate the stability after 100 cycles. Figure S17a–c (Supporting Information) shows that the morphology did not change significantly. Cross-section SEM shows the thickness of EMI-Mo₇₂V₃₀@rGO electrodes before and after cycling (Figure S17d–f, Supporting Information). There is no obvious difference in the thickness between those electrodes, indicating that the electrode did not undergo evident volume vibration during discharge/charge cycling.

The X-ray photoelectron spectroscopy (XPS) was conducted in order to investigate the element valences before and after discharged at 0.01 V to better understand the charge storage mechanism (Figure S18, Supporting Information). In EMI-Mo₇₂V₃₀@rGO electrode, the binding energies of 232.7 and 235.9 eV can be assigned to Mo3d_{3/2} and Mo3d_{5/2}, respectively,

clearly showing that the oxidation state of Mo is +6.^[62] The oxidation state of V are +5 (V2p_{3/2} binding energy of 517.2 eV), and +4 (2p_{3/2} binding energy of 516.1 eV). It might be due to oxidation reaction of the composite during the electrode assembling process. After discharged to 0.01 V versus Li⁺/Li, the oxidation states of Mo and V can be partially reduced to Mo^{IV} and V^{II} due to the appearance of Mo peak and V peak at the binding energy of 230.5 and 513.7 eV, respectively. The above results state that the multiple transition metals in EMI-Mo₇₂V₃₀@rGO anode undergo a redox reaction during the lithiated/delithiated process.

The electrochemical impedance spectroscopies (EIS) were carried out to explain the enhancing electrochemical activity of the composites (Figure S19, Supporting Information). The Nyquist plots possess a depressed semicircle that could be assigned to charge transfer resistances and a slanted line that is related to Li⁺ diffusion ability. The semicircular arc diameter for the

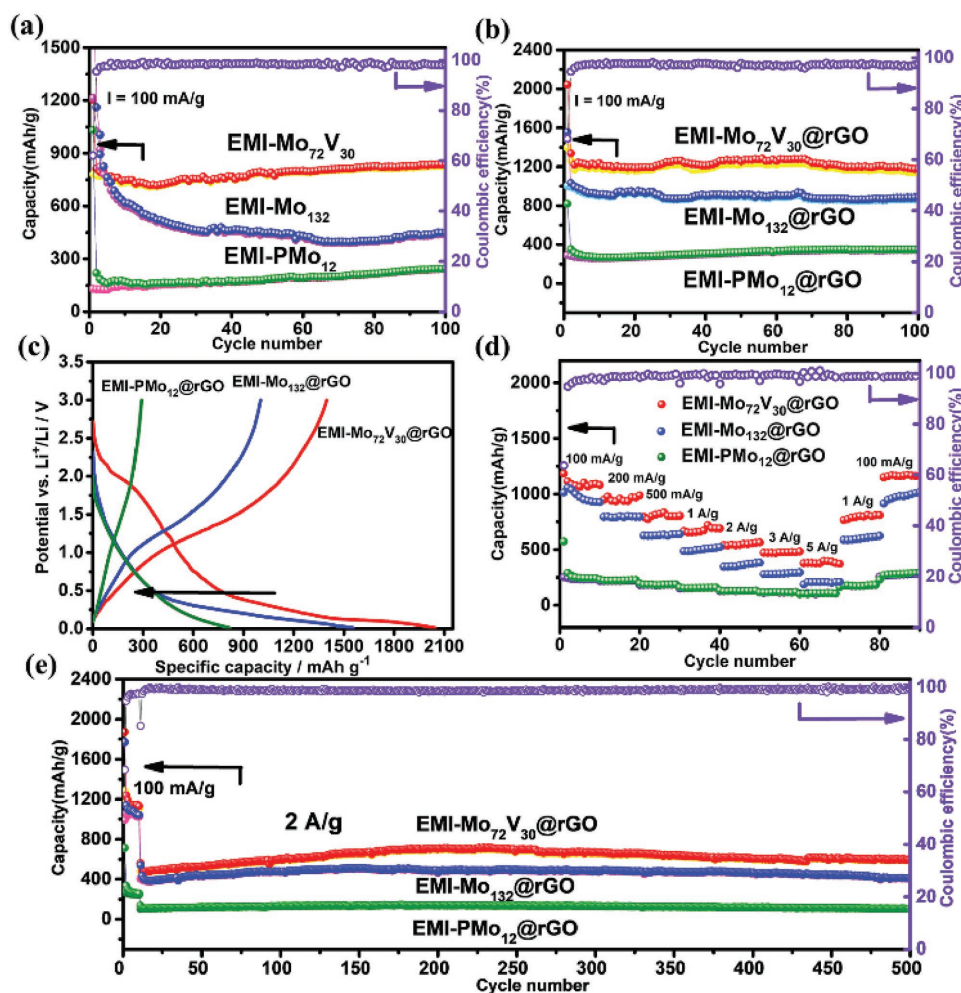


Figure 3. Charge/discharge capacities and columbic efficiency versus cycle number at a current density of 100 mA g⁻¹: a) single crystals EMI-PMo₁₂, EMI-Mo₇₂V₃₀, and EMI-Mo₁₃₂; b) the composites EMI-PMo₁₂@rGO, EMI-Mo₇₂V₃₀@rGO, and EMI-Mo₁₃₂@rGO; c) galvanostatic charge–discharge curves of the composites during the first cycle at current density of 100 mA g⁻¹; d) the cycling performance at various densities; e) the cycling performance at current density of 2 A g⁻¹.

EMI-Mo₇₂V₃₀@rGO in the high-to-medium frequency region is smaller than those for EMI-Mo₇₂V₃₀ and Mo₇₂V₃₀, corresponding to the lower electrolyte resistance (R_s) and charge-transfer resistance (R_{ct}).^[63] It suggests that the favored interaction between electrode and electrolyte interface during cycling improves EMI-Mo₇₂V₃₀@rGO's cycling stability (Table S5, Supporting Information). Furthermore, the Li⁺ diffusion coefficient values (D) are calculated in the Supporting Information with the ratio of $D_{\text{EMI-Mo}_72\text{V}_{30}\text{@rGO}}:D_{\text{EMI-Mo}_72\text{V}_{30}}:D_{\text{Mo}_72\text{V}_{30}}$ being 47.1:1.9:1, demonstrating the remarkably increased Li⁺ migration for EMI-Mo₇₂V₃₀@rGO (Figure S20, Supporting Information).^[64] This result indicates that EMI and rGO do enhance the ionic and electronic conductivity of the electrode material.

EMI-Mo₇₂V₃₀@rGO possesses a reversible capacity over 1100 mAh g⁻¹ at 100 mA g⁻¹, which is higher than the theoretical capacities (detailed calculation can be found in the Supporting Information). In order to understand such high capacity, the kinetics process based on the cyclic voltammetry (CV) profiles at various sweep rates (0.1–10 mV s⁻¹) was further analyzed (Figure S21a, Supporting Information).

In theory, the current (i) at a fixed potential obeys the power-law relationship with scan rate (ν): $I = a\nu^b$.^[65] The adjustable parameter b value can be calculated from the slope of the plots of $\log i$ versus $\log \nu$. The values of b are 0.72 and 0.78 at the corresponding cathodic and anodic peaks, indicating that the diffusion-control and capacitance-control both contribute to the charge storage during the electrochemical process (Figure S21b, Supporting Information).^[66–69] In other words, the composite exhibits a hybrid charge storage mechanism. Therefore, their current response (i) at a given potential (V) is the sum of capacitive contribution ($k_1\nu$) and the diffusion-controlled contribution ($k_2\nu^{0.5}$). By determining k_1 and k_2 , it is possible to determine the current fraction deriving from capacitance and that from Li intercalation at the specific potential.^[70] The ratio of the capacitive-controlled capacity (integrated from the shaded area) is $\approx 38.38\%$ at the scan rate of 0.5 mV s⁻¹, revealing that the diffusion-controlled process takes the majority role in the whole charge storage process (Figure S21c, Supporting Information). However, with different scan rates, the effect of capacitive-controlled process

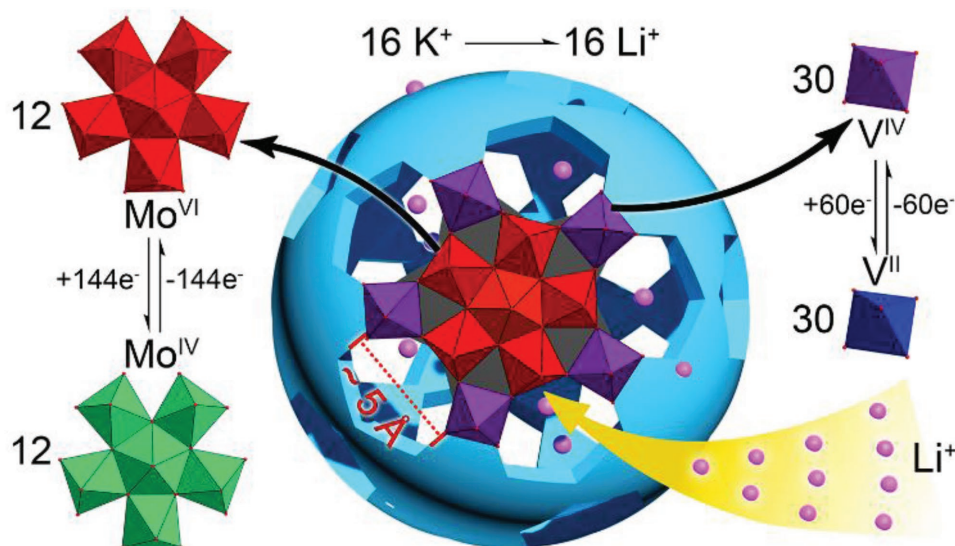


Figure 4. Schematic illustration of the lithiation/delithiation reaction happened in EMI-Mo₇₂V₃₀ molecule.

enlarges as shown in Figure S21d (Supporting Information). Therefore, the capacity of EMI-Mo₇₂V₃₀@rGO results from the cocontribution of the battery (arising from redox of transition metal and cation exchange) and the supercapacitor (arising from the insertion of Li⁺ into the pores of POM or storage of Li⁺ into the interstitial sites between POM and rGO).

3. Discussion

The electrochemical performances of EMI-Mo₇₂V₃₀@rGO are superior to EMI-PMo₁₂@rGO and EMI-Mo₁₃₂@rGO. The reasons are ascribed to: (i) the pore sizes of Mo₇₂V₃₀ and Mo₁₃₂ are bigger than PMo₁₂, in accord with the fact that the density values calculated from the crystal structure of Mo₇₂V₃₀ ($\rho_{\text{calc}} = 2.063 \text{ g cm}^{-3}$) and Mo₁₃₂ ($\rho_{\text{calc}} = 1.928 \text{ g cm}^{-3}$) are smaller than the density of PMo₁₂ ($\rho_{\text{calc}} = 2.193 \text{ g cm}^{-3}$). The larger void space and larger surface area of structure Mo₇₂V₃₀ and Mo₁₃₂ can effectively accommodate the volume variation and charge storage. (ii) It is very interesting to have the macroscopic accumulated situation between molecules from the crystal structure. The shortest distance between Mo₇₂V₃₀ molecules is 2.78 Å, and this is shorter than Mo₁₃₂ (2.87 Å) and PMo₁₂ (2.99 Å). It can be concluded that electrode materials with close packing distance and shorten diffusion length can provide faster transport pathways for both electrons and Li⁺. (iii) Both Mo₁₃₂ and Mo₇₂V₃₀ contain 12 {(Mo^{VI})Mo^{VI}₅} pentagonal bipyramids, whereas the 30 linkers are {V^{IV}O} in Mo₇₂V₃₀ and {Mo₂V^{IV}O₁₁} in Mo₁₃₂, respectively. Although they are isostructural Keplrate structures, the redox ability of V^{IV} is much stronger than Mo^V. (iv) EMI-Mo₇₂V₃₀ is a highly stable giant POM, and has 102 transition metal oxides {Mo^{VI}O₆} and {V^{IV}O} in total in one molecular. The maximum number of the transferred electrons happened in element valence changes during the redox reactions is 204 (72 Mo^{VI} to Mo^{IV} and 30 V^{IV} to V^{II}) (Figure 4). The 16 K⁺ ions were partially occupied in the entrance of the 20 {Mo₃V₃O₉} pores (diameter

of $\approx 5 \text{ Å}$) in each Mo₇₂V₃₀ molecule and could function as a door allowing opening and closing during the charge/discharge process (Figure S22, Supporting Information). After the Li⁺ insertion process, the K⁺ could be substituted by Li⁺, and then the reaction undergoes a reversible process during delithiation process. Although POM state becomes amorphous during the Li⁺ insertion/extraction,^[71] the POM structures do not change. In comparison, there are 20 {Mo₉O₉}-type pores in Mo₁₃₂, but the pores are open and big enough for Li⁺, which might be more conducive to Li⁺ overflow and not facilitated for Li⁺ storage. Mo₇₂V₃₀ possesses such characteristics that are favorable for Li⁺ transfer and enable good capacity and long-term cycling.

4. Conclusion

In summary, we have successfully utilized POM models to simulate the solid-to-hollow structure in solid-state battery materials. The composites EMI-PMo₁₂@rGO, EMI-Mo₇₂V₃₀@rGO, and EMI-Mo₁₃₂@rGO were synthesized and their Li⁺ storage mechanisms were studied to illustrate that the hollow materials can provide more efficient lithium-ion storage than solid sphere at the molecular or atomic level for the first time. Giant POM as LIBs was first studied here, showing advantages over the traditional transition oxides with similar structural moieties due to the inherent nature of the multiple redox centers within the crystalline structure. The fullerene-type composite EMI-Mo₇₂V₃₀@rGO delivers an enhanced capacity of over 1100 mA h g⁻¹ at 100 mA g⁻¹ and a long cycle life over 500 cycles. It is one of the best battery performances among the reported POM-based electrodes. Besides the innate open pore within the structure can not only buffer the volume expansion but also show cocontributed capacity in-between a battery and a supercapacitor. The novel materials we have synthesized here are promising for extending their study in sodium batteries, lithium-air batteries, fuel cells, and so on.

Supporting Information

Supporting Information is available from the Wiley Online Library or from the author.

Acknowledgements

This work was financially supported by the National Natural Science Foundation of China (Nos. 21701086 and 21471003), the Postdoctoral Science Foundation of China (No. 2017M621775), and Jiangsu Postdoctoral Research Funds (No. 1701116C). The authors thank the staff from BL17B beamline of National Facility for Protein Science Shanghai (NFPS) at Shanghai Synchrotron Radiation Facility, for assistance during data collection.

Conflict of Interest

The authors declare no conflict of interest.

Keywords

lithium-ion storage, polyoxometalates, single crystals, superstable

Received: May 22, 2018
Revised: June 26, 2018
Published online: July 30, 2018

- [1] J. M. Tarascon, M. Armand, *Nature* **2001**, 414, 359.
- [2] B. Dunn, H. Kamath, J. M. Tarascon, *Science* **2011**, 334, 928.
- [3] X. Han, W.-M. Chen, X. Han, Y.-Z. Tan, D. Sun, *J. Mater. Chem. A* **2016**, 4, 13040.
- [4] H. Liu, X. Liu, W. Li, X. Guo, Y. Wang, G. Wang, D. Zhao, *Adv. Energy Mater.* **2017**, 7, 1700283.
- [5] Y. Guo, H. Li, T. Zhai, *Adv. Mater.* **2017**, 29, 1700007.
- [6] X.-B. Cheng, M.-Q. Zhao, C. Chen, A. Pentecost, K. Maleski, T. Mathis, X.-Q. Zhang, Q. Zhang, J. Jiang, Y. Gogotsi, *Nat. Commun.* **2017**, 8, 336.
- [7] R. Zhang, X.-R. Chen, X. Chen, X.-B. Cheng, X.-Q. Zhang, C. Yan, Q. Zhang, *Angew. Chem., Int. Ed.* **2017**, 56, 7764.
- [8] Y. Chu, L. Guo, B. Xi, Z. Feng, F. Wu, Y. Lin, J. Liu, D. Sun, J. Feng, Y. Qian, S. Xiong, *Adv. Mater.* **2017**, 30, 1704244.
- [9] F. Wang, H.-Y. Zhuo, X. Han, W.-M. Chen, D. Sun, *J. Mater. Chem. A* **2017**, 5, 22964.
- [10] F. Wu, S. Zhang, B. Xi, Z. Feng, D. Sun, X. Ma, J. Zhang, J. Feng, S. Xiong, *Adv. Energy Mater.* **2018**, 8, 1703242.
- [11] N. Kuwata, J. Kawamura, K. Toribami, T. Hattori, N. Sata, *Electrochem. Commun.* **2004**, 6, 417.
- [12] J. Morales, L. Sanchez, F. Martin, F. Berry, X. Ren, *J. Electrochem. Soc.* **2005**, 152, A1748.
- [13] L. Shi, Y. D. He, X. H. Xia, Z. M. Jian, H. B. Liu, *J. Iran. Chem. Soc.* **2010**, 7, 721.
- [14] Z. Ding, L. Zhao, L. Suo, Y. Jiao, S. Meng, Y.-S. Hu, Z. Wang, L. Chen, *Phys. Chem. Chem. Phys.* **2011**, 13, 15127.
- [15] S. H. Lee, S.-H. Yu, J. E. Lee, A. Jin, D. J. Lee, N. Lee, H. Jo, K. Shin, T.-Y. Ahn, Y.-W. Kim, H. Choe, Y.-E. Sung, T. Hyeon, *Nano Lett.* **2013**, 13, 4249.
- [16] F. Wu, S. Xiong, Y. Qian, S. H. Yu, *Angew. Chem., Int. Ed.* **2015**, 54, 10787.
- [17] X. Wang, X.-L. Wu, Y.-G. Guo, Y. Zhong, X. Cao, Y. Ma, J. Yao, *Adv. Funct. Mater.* **2010**, 20, 1680.
- [18] W. Guo, W. Sun, Y. Wang, *ACS Nano* **2015**, 9, 11462.
- [19] L. Zhou, D. Zhao, X. W. Lou, *Adv. Mater.* **2012**, 24, 745.
- [20] S. Xu, C. M. Hessel, H. Ren, R. Yu, Q. Jin, M. Yang, H. Zhao, D. Wang, *Energy Environ. Sci.* **2014**, 7, 632.
- [21] X. Wu, G. Q. Lu, L. Wang, *Energy Environ. Sci.* **2011**, 4, 3565.
- [22] H. Ren, R. Yu, J. Wang, Q. Jin, M. Yang, D. Mao, D. Kisailus, H. Zhao, D. Wang, *Nano Lett.* **2014**, 14, 6679.
- [23] Y. Zhao, L. Jiang, *Adv. Mater.* **2009**, 21, 3621.
- [24] C. C. Li, Q. H. Li, L. B. Chen, T. H. Wang, *ACS Appl. Mater. Interfaces* **2012**, 4, 1233.
- [25] Z. Wang, L. Zhou, X. W. Lou, *Adv. Mater.* **2012**, 24, 1903.
- [26] X. Lai, J. E. Halpert, D. Wang, *Energy Environ. Sci.* **2012**, 5, 5604.
- [27] X. Li, L. Zhi, *Nanoscale* **2013**, 5, 8864.
- [28] L. Zhang, H. B. Wu, X. W. Lou, *Adv. Energy Mater.* **2014**, 4, 1300958.
- [29] M. Sasidharan, K. Nakashima, *Acc. Chem. Res.* **2014**, 47, 157.
- [30] R. Purbia, S. Paria, *Nanoscale* **2015**, 7, 19789.
- [31] X. Wang, J. Feng, Y. Bai, Q. Zhang, Y. Yin, *Chem. Rev.* **2016**, 116, 10983.
- [32] S.-H. Yu, S. H. Lee, D. J. Lee, Y.-E. Sung, T. Hyeon, *Small* **2016**, 12, 2146.
- [33] J. Wang, H. Tang, L. Zhang, H. Ren, R. Yu, Q. Jin, J. Qi, D. Mao, M. Yang, Y. Wang, P. Liu, Y. Zhang, Y. Wen, L. Gu, G. Ma, Z. Su, Z. Tang, H. Zhao, D. Wang, *Nat. Energy* **2016**, 1, 16050.
- [34] L. Zhou, Z. Zhuang, H. Zhao, M. Lin, D. Zhao, L. Mai, *Adv. Mater.* **2017**, 29, 1602914.
- [35] X. Wang, K. Chen, G. Wang, X. Liu, H. Wang, *ACS Nano* **2017**, 11, 11602.
- [36] L. Yu, H. B. Wu, X. W. D. Lou, *Acc. Chem. Res.* **2017**, 50, 293.
- [37] M. Wang, Y. Huang, X. Chen, K. Wang, H. Wu, N. Zhang, H. Fu, *J. Alloys Compd.* **2017**, 691, 407.
- [38] B. Y. Guan, X. W. D. Lou, X. Y. Yu, H. B. Wu, *Adv. Mater.* **2017**, 29, 1703614.
- [39] Y. Lu, L. Yu, M. Wu, Y. Wang, X. W. Lou, *Adv. Mater.* **2018**, 30, 1702875.
- [40] S. S. Mal, U. Kortz, *Angew. Chem., Int. Ed.* **2005**, 44, 3777.
- [41] H. N. Miras, J. Yan, D. L. Long, L. Cronin, *Chem. Soc. Rev.* **2012**, 41, 7403.
- [42] H. Yang, T. Song, L. Liu, A. Devadoss, F. Xia, H. Han, H. Park, W. Sigmund, K. Kwon, U. Paik, *J. Phys. Chem. C* **2013**, 117, 17376.
- [43] J.-J. Chen, M. D. Symes, S.-C. Fan, M.-S. Zheng, H. N. Miras, Q.-F. Dong, L. Cronin, *Adv. Mater.* **2015**, 27, 4649.
- [44] R.-W. Huang, Y.-S. Wei, X.-Y. Dong, X.-H. Wu, C.-X. Du, S.-Q. Zang, T. C. W. Mak, *Nat. Chem.* **2017**, 9, 689.
- [45] Z. Li, X.-X. Li, T. Yang, Z.-W. Cai, S.-T. Zheng, *Angew. Chem., Int. Ed.* **2017**, 56, 2664.
- [46] X. Chen, Z. Wang, R. Zhang, L. Xu, D. Sun, *Chem. Commun.* **2017**, 53, 10560.
- [47] A. Müller, E. Krickemeyer, H. Bögge, M. Schmidtman, F. Peters, *Angew. Chem., Int. Ed.* **1998**, 37, 3359.
- [48] M. T. Pope, U. Kortz, *Encyclopedia of Inorganic and Bioinorganic Chemistry*, Wiley, Hoboken, NJ, USA **2012**.
- [49] Y. Ji, L. Huang, J. Hu, C. Streb, Y.-F. Song, *Energy Environ. Sci.* **2015**, 8, 776.
- [50] Y.-J. Tang, M.-R. Gao, C.-H. Liu, S.-L. Li, H.-L. Jiang, Y.-Q. Lan, M. Han, S.-H. Yu, *Angew. Chem., Int. Ed.* **2015**, 54, 12928.
- [51] N. Kawasaki, H. Wang, R. Nakanishi, S. Hamanaka, R. Kitaura, H. Shinohara, T. Yokoyama, H. Yoshikawa, K. Awaga, *Angew. Chem., Int. Ed.* **2011**, 50, 3471.
- [52] H. Wang, S. Hamanaka, Y. Nishimoto, S. Irle, T. Yokoyama, H. Yoshikawa, K. Awaga, *J. Am. Chem. Soc.* **2012**, 134, 4918.
- [53] J. Hu, Y. Ji, W. Chen, C. Streb, Y.-F. Song, *Energy Environ. Sci.* **2016**, 9, 1095.
- [54] J. Xie, Y. Zhang, Y. Han, C. Li, *ACS Nano* **2016**, 10, 5304.
- [55] Y.-J. Tang, Y. Wang, X.-L. Wang, S.-L. Li, W. Huang, L.-Z. Dong, C.-H. Liu, Y.-F. Li, Y.-Q. Lan, *Adv. Energy Mater.* **2016**, 6, 1600116.

- [56] J. Liu, Z. Chen, W. Xuan, S. Chen, B. Zhang, J. Wang, H. Wang, B. Tian, M. Chen, X. Fan, Y. Huang, T. C. Sum, J. Lin, Z. X. Shen, *ACS Nano* **2017**, *11*, 6911.
- [57] T. Wei, M. Zhang, P. Wu, Y.-J. Tang, S.-L. Li, F.-C. Shen, X.-L. Wang, X.-P. Zhou, Y.-Q. Lan, *Nano Energy* **2017**, *34*, 205.
- [58] S. Herrmann, M. Kostrzewa, A. Wierschem, C. Streb, *Angew. Chem., Int. Ed.* **2014**, *53*, 13596.
- [59] S. Baldelli, J. Bao, W. Wu, S. S. Pei, *Chem. Phys. Lett.* **2011**, *516*, 171.
- [60] J. Hu, H. Diao, W. Luo, Y.-F. Song, *Chem. Eur. J.* **2017**, *23*, 8729.
- [61] B. Botar, P. Kogerler, C. L. Hill, *Chem. Commun.* **2005**, 3138.
- [62] J. C. Vedrine, H. Praliaud, P. Meriaudeau, M. Che, *Surf. Sci.* **1979**, *80*, 101.
- [63] Y. Dai, Q. Li, S. Tan, Q. Wei, Y. Pan, X. Tian, K. Zhao, X. Xu, Q. An, L. Mai, Q. Zhang, *Nano Energy* **2017**, *40*, 73.
- [64] N. Kumagai, H. Kitamoto, M. Baba, S. Durand-Vidal, D. Devilliers, H. Groult, *J. Appl. Electrochem.* **1998**, *28*, 41.
- [65] X.-Y. Yang, T. Wei, J.-S. Li, N. Sheng, P.-P. Zhu, J.-Q. Sha, T. Wang, Y.-Q. Lan, *Inorg. Chem.* **2017**, *56*, 8311.
- [66] V. Augustyn, P. Simon, B. Dunn, *Energy Environ. Sci.* **2014**, *7*, 1597.
- [67] P. Simon, Y. Gogotsi, B. Dunn, *Science* **2014**, *343*, 1210.
- [68] Y. Han, M. Yang, Y. Zhang, J. Xie, D. Yin, C. Li, *Chem. Mater.* **2016**, *28*, 3139.
- [69] M. R. Lukatskaya, B. Dunn, Y. Gogotsi, *Nat. Commun.* **2016**, *7*, 12647.
- [70] Y. Wang, Y. Song, Y. Xia, *Chem. Soc. Rev.* **2016**, *45*, 5925.
- [71] E. Ni, S. Uematsu, Z. Quan, N. Sonoyama, *J. Nanopart. Res.* **2013**, *15*, 1732.